NeuroImage 276 (2023) 120212

Contents lists available at ScienceDirect

NeuroImage

journal homepage: www.elsevier.com/locate/neuroimage

Structural basis of envelope and phase intrinsic coupling modes in the cerebral cortex

Arnaud Messé[a,*], Karl J. Hollensteiner[b], Céline Delettre[a,c], Leigh-Anne Dell-Brown[a], Florian Pieper[b], Lena J. Nentwig[a], Edgar E. Galindo-Leon[b], Benoît Larrat[d], Sébastien Mériaux[d], Jean-François Mangin[d], Isabel Reillo[e], Camino de Juan Romero[e], Víctor Borrell[e], Gerhard Engler[b], Roberto Toro[c,f], Andreas K. Engel[b,1], Claus C. Hilgetag[a,g,1]

[a] *Institute of Computational Neuroscience, Hamburg Center of Neuroscience, University Medical Center Hamburg-Eppendorf, Hamburg University, Martinistraße 52, Hamburg 20246, Germany*

[b] *Department of Neurophysiology and Pathophysiology, Hamburg Center of Neuroscience, University Medical Center Hamburg-Eppendorf, Hamburg University, Martinistraße 52, Hamburg 20246, Germany*

[c] *Unité de Neuroanatomie Appliquée et Théorique, Unité de Génétique Humaine et Fonctions Cognitives, Institut Pasteur, Université Paris Cité, 25-28 rue du Dr Roux, Paris 75015, France*

[d] *NeuroSpin, CEA, Paris-Saclay University, Centre d'études de Saclay, Bâtiment 145, Gif-sur-Yvette 91191, France*

[e] *Developmental Neurobiology Unit, Instituto de Neurociencias, Consejo Superior de Investigaciones Científicas - Universidad Miguel Hernández, Sant Joan d'Alacant, Av. Santiago Ramón y Cajal s/n, Sant Joan d'Alacant 03550, Spain*

[f] *Center for Research and Interdisciplinarity, Paris Descartes University, 24, rue du Faubourg Saint Jacques, Paris 75014, France*

[g] *Department of Health Sciences, Boston University, 635 Commonwealth Avenue, Boston, Massachusetts 02215, USA*

ARTICLE INFO

Keywords:
Ferret brain
Intrinsic coupling modes
Structure–function relationship
Time delay

ABSTRACT

Intrinsic coupling modes (ICMs) can be observed in ongoing brain activity at multiple spatial and temporal scales. Two families of ICMs can be distinguished: phase and envelope ICMs. The principles that shape these ICMs remain partly elusive, in particular their relation to the underlying brain structure. Here we explored structure-function relationships in the ferret brain between ICMs quantified from ongoing brain activity recorded with chronically implanted micro-ECoG arrays and structural connectivity (SC) obtained from high-resolution diffusion MRI tractography. Large-scale computational models were used to explore the ability to predict both types of ICMs. Importantly, all investigations were conducted with ICM measures that are sensitive or insensitive to volume conduction effects. The results show that both types of ICMs are significantly related to SC, except for phase ICMs when using measures removing zero-lag coupling. The correlation between SC and ICMs increases with increasing frequency which is accompanied by reduced delays. Computational models produced results that were highly dependent on the specific parameter settings. The most consistent predictions were derived from measures solely based on SC. Overall, the results demonstrate that patterns of cortical functional coupling as reflected in both phase and envelope ICMs are both related, albeit to different degrees, to the underlying structural connectivity in the cerebral cortex.

1. Introduction

Intrinsic coupling modes reflect the patterns of synchronization or functional connectivity (FC) between neuronal ensembles during spontaneous brain activity (Engel et al., 2013). These coupling modes represent a widely used concept in modern neuroscience for probing the connectional organization of intact or damaged brains. ICMs have been associated with individual brain characteristics such as behavior and cognitive abilities (Fox and Raichle, 2007; Fries, 2005; Hipp et al., 2011; Smith et al., 2015), and aberrant ICM patterns have been linked to a variety of brain diseases (Fornito and Bullmore, 2015; Schnitzler and Gross, 2005; Uhlhaas and Singer, 2012). Numerous studies in animals and humans have suggested that ICMs occur across a broad range of spatial and temporal scales, involving two distinct families of dynam-

---

Abbreviations: ICMs, Intrinsic coupling modes; FC, Functional connectivity; SC, Structural connectivity; ECoG, Electrocorticography; eICMs, Envelope ICMs; pICMs, Phase ICMs.

[*] Corresponding author.

E-mail address: a.messe@uke.de (A. Messé).

[1] These authors contributed equally to this work.

https://doi.org/10.1016/j.neuroimage.2023.120212.
Received 9 December 2022; Received in revised form 9 May 2023; Accepted 30 May 2023
Available online 1 June 2023.
1053-8119/© 2023 The Author(s). Published by Elsevier Inc. This is an open access article under the CC BY-NC-ND license (http://creativecommons.org/licenses/by-nc-nd/4.0/)

ical coupling modes, namely phase ICMs (pICMs) and envelope ICMs (eICMs) (Engel et al., 2013). Phase ICMs represent ongoing oscillations of band-limited dynamics, typically occurring at frequencies between about 1 to 150 Hz, which can be quantified by measures of phase consistency. By contrast, envelope ICMs correspond to coupled aperiodic fluctuations, typically on slower time scales, which can be uncovered by the correlation of signal power envelopes. However, the principles that shape both types of ICMs remain partly unresolved, notably their relation to the underlying brain structure (Honey et al., 2010; Park and Friston, 2013). Therefore, a careful investigation of the relation of ICMs to structural connectivity is required in order to advance our understanding of the network basis of cognition and behavior (Deco et al., 2011; Hipp et al., 2012; Park and Friston, 2013; Siegel et al., 2012; Singer, 2013; Sporns, 2014).

The physical basis for the emergence of functional connectivity patterns is the underlying brain anatomy, specifically, structural connectivity among brain regions (Foster et al., 2016). In this context, diffusion MRI has transformed the field by its ability to estimate the whole brain architecture of structural connections in a non-invasive way (Le Bihan and Heidi, 2011). In parallel, resting-state fMRI has become a popular approach for probing the functional organization of the brain at slow time scales, representing eICMs (van den Heuvel and Pol, 2010; Raichle, 2010). Pioneering studies have demonstrated a tight intricate association between SC patterns and resting-state fMRI-based FC (Greicius et al., 2009; Hagmann et al., 2008; Koch et al., 2002; Vincent et al., 2007). Much less well understood are interactions at faster time scales, that is, pICMs, and their relations to the underlying anatomy. Nonetheless, a few studies have reported a positive association between pICMs and SC, using electrophysiological measurements (Chu et al., 2015; Meier et al., 2016). However, a comprehensive description of the structure-function relationships including both types of ICMs and across frequency ranges is lacking.

Despite significant progress made in the analysis of functional neuroimaging data, such measurements suffer from diverse limitations. While fMRI has a good spatial resolution, its temporal resolution is rather limited, while the opposite is true for electrophysiological data. Furthermore, electrophysiological recordings are prone to reveal artefactual functional connectivity caused by the mixing of cortical signals at the sensor level due to volume conduction effects (Haufe et al., 2013). Because volume conduction is instantaneous (zero-lag), a number of measures quantifying only lagged couplings or strategies that explicitly remove zero-lag couplings have been designed to tackle this issue (‘lagged ICMs’) (Palva and Palva, 2012). However, such measures have rarely been employed in the investigation of structure-function relationships (but see Finger et al., 2016).

Large-scale computational models have offered new mathematical tools to explicitly link SC to ICMs and to highlight generative models of functional coupling (Breakspear, 2017; Deco et al., 2009; 2008). Most computational models presented in recent years have focused on describing functional interactions at slow time scales (eICMs) using resting-state fMRI (Cabral et al., 2014a). A variety of models have been developed for this purpose that specifically consider the influence of a variety of parameters such as structural weights, delays and noise on neural dynamics (Cabral et al., 2014a; Deco et al., 2011; 2009). Remarkably, substantially different computational models result in similar FC predictions (Messé et al., 2014; 2015b), in such a way that simple statistical models based on the topological characteristics of SC can be used with similar levels of prediction performance (Goñi et al., 2014; Messé et al., 2015a). Few studies have extended this framework by using electrophysiological measurements (Abeysuriya et al., 2018; Cabral et al., 2014b; Tewarie et al., 2019). Recent investigations suggest that neuronal synchronization at faster time scales (pICMs) can also be predicted by computational simulations (Abeysuriya et al., 2018; Finger et al., 2016). Yet, the relative ability of computational models to predict both types of ICMs remains elusive, especially when using lagged ICM measures. Overall, the mechanisms underlying the two types of ICMs are only partly resolved.

Against this background, we used data of ongoing activity of multiple cortical areas recorded from awake ferrets with chronically implanted micro-ECoG arrays (Stitt et al., 2017). Such a setting provides recordings with high temporal and spatial resolution for a substantial number of cortical areas. Moreover, due to the low gyrification of the ferret brain and the close proximity of the electrodes to the brain, volume conduction is strongly reduced, compared to non-invasive approaches such as MEG/EEG (Dubey and Ray, 2019; Einevoll et al., 2013; Liu et al., 2015). Additionally, we obtained structural connectivity estimates from diffusion MRI tractography data for the regions underlying the micro-ECoG array (Delettre et al., 2019). We found that both types of ICMs partially reflect the underlying SC, that the correlation with SC increases with increasing carrier frequency, and that pICMs and eICMs show resemblance in their topographies, pointing to a mechanistic anchoring of the ICMs in the underlying SC. However, the use of lagged ICMs virtually abolishes the association of pICMs with SC except for high frequency, while the association of eICMs with SC remains unchanged. The strengthening of the structure-function association with frequency is accompanied by a decrease in time delays. Also, we found that computational models, independently of their complexity, can reproduce ICM patterns reasonably well, but not much beyond SC alone. Thus, the results demonstrate that patterns of cortical functional coupling, as reflected in both phase and envelope ICMs, are both characteristically constrained, albeit to different degrees, by the underlying structural connectivity in the cerebral cortex.

2. Material and methods

2.1. ECoG data

Intrinsic coupling modes were extracted from micro-ECoG recordings of ongoing brain activity in awake ferrets (*Mustela putorius furo*). Data were collected in five adult female ferrets (Stitt et al., 2017). All experiments were approved by the Hamburg state authority for animal welfare and were performed in accordance with the guidelines of the German Animal Protection Law.

To obtain the recordings from an extended set of cortical areas in freely moving animals, a micro-ECoG array had been implanted that was co-developed with the University of Freiburg (IMTEK, Freiburg) (Rubehn et al., 2009). The array covered a large portion of the posterior, parietal, and temporal surface of the left ferret brain hemisphere. Sixty-four platinum electrodes (∅ 250 μm) were arranged equidistantly (1.5 mm) in a hexagonal manner. See Fig. 1 for a schematic diagram of the micro-ECoG layout. Ferrets had been accustomed to a recording box (45×20×52 cm), where they could move around freely while neural activity was recorded. For each animal, at least 4 separate recording sessions with a duration of at least 2 h had been obtained. Micro-ECoG signals had been recorded using a 64 channel AlphaLab SnRTM recording system (Alpha Omega Engineering, Israel), filtered (0.1–357 Hz bandpass), and digitized (1.4 kHz sampling rate). A total of 23 recording sessions were obtained and analysed.

To reduce noise and also attenuate volume conduction effects, a local Laplacian montage was used (Tenke and Kayser, 2012) also called current source density (Pesaran et al., 2018). For each electrode, the average signal within its neighborhood (maximal distance of 2 mm) was subtracted (Hjorth, 1975). Noise epochs were detected using a threshold of 10 standard deviations. Data were rejected in a window of ± 10 s from all time points that exceeded this threshold. Then, notch filters were applied to remove line noise and its harmonics (50, 100, and 150 Hz), and the data were downsampled to 500 Hz. All data were visually inspected before further analysis to exclude electrical artefacts. In a previous study, brain activity was objectively classified into slow-wave sleep, rapid-eye-movement sleep and awake periods, using a data-driven approach (Stitt et al., 2017). The present study focused only on data from

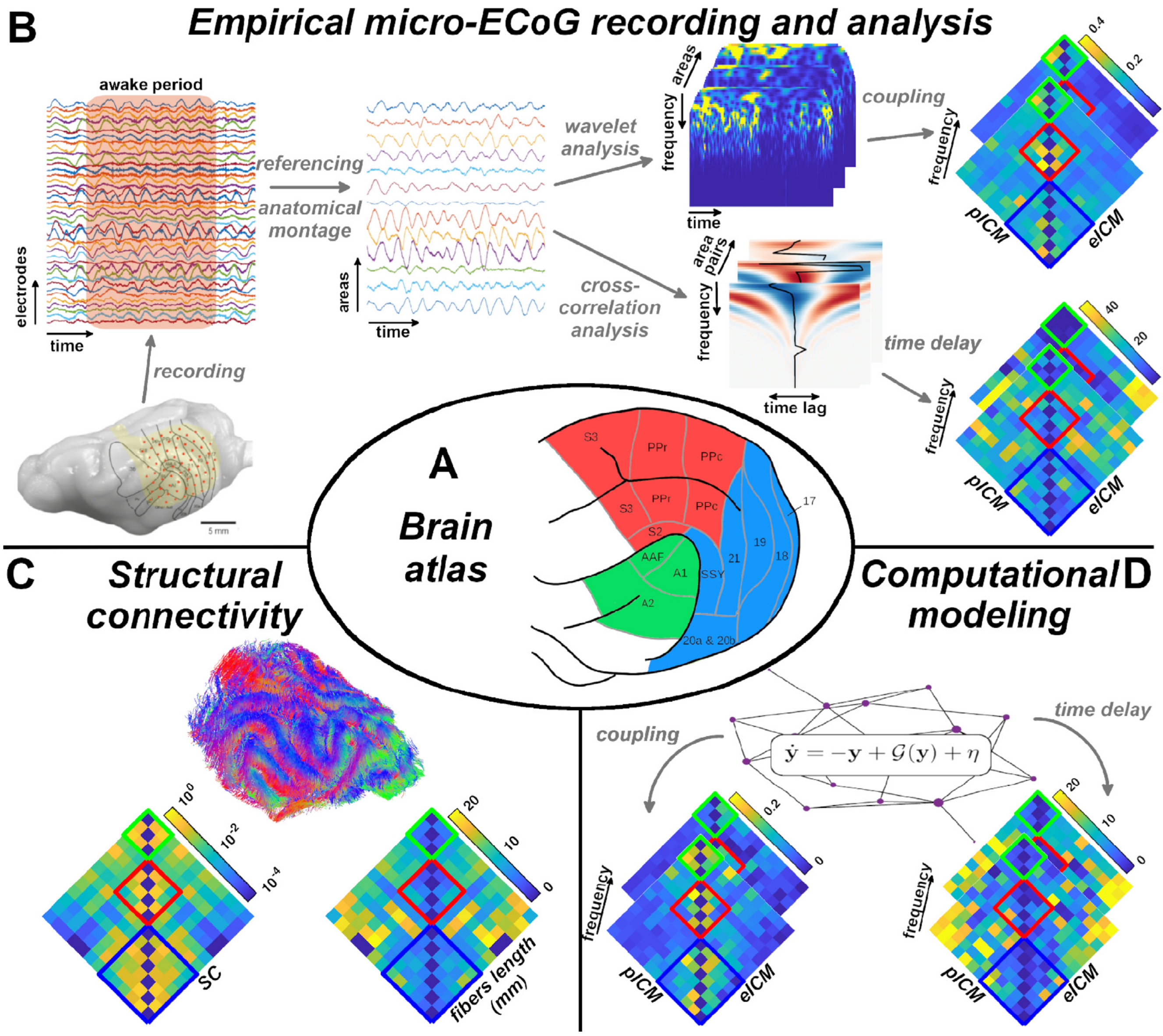
B
Empirical micro-ECoG recording and analysis
awake period
electrodes
time
referencing
anatomical montage
areas
time
wavelet analysis
areas
frequency
time
coupling
frequency
0.4
0.2
0
pICM
eICM
cross-correlation analysis
area pairs
frequency
time lag
time delay
frequency
40
20
0
pICM
eICM
recording
5 mm
A
Brain atlas
S3
PPr
PPc
S3
PPr
PPc
S2
AAF
A1
A2
SSY
21
19
18
17
20a & 20b
C
Structural connectivity
10^0
10^{-2}
10^{-4}
SC
20
10
0
fibers length (mm)
Computational modeling
D
coupling
$\dot{\mathbf{y}} = -\mathbf{y} + \mathcal{G}(\mathbf{y}) + \eta$
time delay
0.2
0
frequency
pICM
eICM
20
10
0
frequency
pICM
eICM

Fig. 1. Multimodal processing pipeline. (A) Ferret posterior cerebral cortex parcellated into 13 functionally and anatomically distinct regions according to Bizley and King (2009). Abbreviations: S2, S3: somatosensory cortex 2 and 3; PPr/c: rostral/caudal posterior parietal cortex; 17, 18, 19, 20, 21: occipital visual cortex areas; SSY: suprasylvian field; A1, A2: primary and secondary auditory cortex; AAF: anterior auditory field. (B) Empirical micro-ECoG recording and analysis. (From left to right) Micro-ECoG-array over the left posterior ferret brain cortex. Awake periods were extracted from the resulting brain activity, electrodes were re-referenced and mapped onto the ferret brain atlas, then time-frequency representations were computed using wavelet transforms for each area and cross-correlation were computed across frequencies for each pair of areas. Subsequently, phase and envelope ICMs and their delays were computed over multiple frequencies and between all pairs of areas, and averaged within frequency bands. (C) Patterns of structural connectivity extracted from diffusion MRI tractography and the associated fibers length. (D) Large-scale computational brain models and an illustrative example of simulated ICMs and their delays.

awake periods with, on average, 34 periods of 78 s per session across animals (periods shorter than 10 s were discarded to increase statistical power).

To account for inter-individual differences in the position of the micro-ECoG array and thus make cross-animal comparisons possible, micro-ECoG electrodes were monted at the area-level using the atlas of Bizley and King (2009). The position of micro-ECoG grids were projected onto a scaled illustration of the atlas of Bizley and King (2009). Each electrode was assigned to a cortical area by a 'winner-takes-all' method using its maximum overlap, and subsequently the signals of the electrodes belonging to a given area were averaged. In parallel, the distance between electrodes were also averaged within and between areas and subsequently averaged across animals. This physical distance matrix was used as a control in the subsequent analysis. In total, 13 areas were covered by the micro-ECoG array for all animals (Fig. 1).

In order to have a condensed representation of the connectivity analyses, we defined frequency bands of interest. Given the variability of the frequency peaks classically encountered in the literature together with a lack of consensus in the definition of the frequency bands, we resorted to a data-driven approach based on the power spectrum. We calculated the power spectral densities, for each awake period, using mutlitaper based on the Slepian sequences (DPSS) on windowed segments of 10 s with 50% overlap. Then, the FOOOF method was used to detect the oscillatory peaks over the 1/f component of the power spectra (Donoghue et al., 2020). This allowed us to compute the distribution of those peaks over all awake periods of all animals. Consequently, we defined 4 frequency bands, which encompass the dominant oscillatory modes: 3–6 Hz (θ); 9–20 Hz (β_1); 20–35 Hz (β_2); and 55–145 Hz (γ), see Fig. S1.

For each animal and each awake period, a time-frequency estimate $X_i(t,f)$ of signal $x_i(t)$ at area i was computed by convolution with a series of Morlet's wavelets. Carrier frequencies were spaced logarithmically from 0.5 to 200 Hz. The width of the wavelets was set to 7 cycles. Spectral estimates were computed at a rate of 5 Hz. Then, phase and envelope ICMs were computed between all pairs of areas using the measures of phase locking and power correlation, respectively, see Intrinsic coupling modes section. Time delays were computed using windowed cross-correlation, see Time delays section. Subsequently, ICM matrices were averaged within the frequency bands. Finally, ICM matrices were averaged across awake periods within each session per animal (session-level), then across sessions within each animal (animal-level), and also across animals (group-level). Results on the animal- and group-levels are presented in the main text, while results on the session-level are reported in supplementary figures.

All data analysis was performed using custom scripts for Matlab (Mathworks Inc) and the Fieldtrip software (Oostenveld et al., 2011).

2.2. Intrinsic coupling modes

Phase and envelope ICMs were estimated using the measures of phase locking and power envelope correlation, respectively. Phase locking value is a measure of the linear relationship between the phase of oscillatory signals over time (Lachaux et al., 1999), also called mean phase coherence (Mormann et al., 2000), where a high value corresponds to signals with aligned phases. The phase locking value between signals at location i and j and for frequency f, is given by

$$PLV_{ij}(f) = \frac{1}{T}\left|\sum_{t=1}^{T} e^{-i\left[\phi_i(t,f)-\phi_j(t,f)\right]}\right|, \tag{1}$$

where T is the data length, and $\phi_i(t,f) = arg(X_i(t,f))$ the phase of signal i at time t and frequency f.

Power correlation is a measure of the similarity between the power envelopes of the recorded signals (Brookes et al., 2011; Hipp et al., 2012; de Pasquale et al., 2012). Power envelope is given by the squared absolute values of the complex spectral estimates. Furthermore, a logarithmic transform was applied to render the statistics more normal. Then, the Pearson correlation between the resulting power envelopes from two different locations i and j was computed

$$PEC_{ij}(f) = corr(\log(|X_i(t,f)|^2), \log(|X_j(t,f)|^2)). \tag{2}$$

Alternatively, we also explored measures robust to volume conduction effects. To this end, phase and envelope ICMs were estimated using the imaginary phase locking and orthogonal power envelope correlation, respectively. Following the logic of the imaginary coherence (Nolte et al., 2004), imaginary phase locking represents the imaginary part of the average phase difference, which effectively eliminates the contribution of volume-conducted signals by exclusively considering phase-lagged signal components

$$iPLV_{ij}(f) = \frac{1}{T}\mathfrak{I}\left\{\sum_{t=1}^{T} e^{-i\left[\phi_i(t,f)-\phi_j(t,f)\right]}\right\}. \tag{3}$$

Orthogonal power envelope correlation, similar to imaginary phase locking, removes instantaneous covariations by orthogonalizing signals before computing their power envelopes (Brookes et al., 2012; Hipp et al., 2012). The time-frequency estimate $X_i(t,f)$ orthogonalized with respect to signal $X_j(t,f)$ is given by

$$X_{i\perp j}(t,f) = \mathfrak{I}\left(X_i(t,f)\frac{X_j^*(t,f)}{|X_j(t,f)|}\right). \tag{4}$$

The orthogonalization being not symmetric, $X_{i\perp j}(t,f) \neq X_{j\perp i}(t,f)$, power envelope correlation was computed in both directions and subsequently averaged.

2.3. Time delays

Similar preprocessing steps as for the ICM measures were applied to compute time delays except that the data were downsampled to 1000 Hz (to obtain finer time resolution). For each animal and each awake period, areas' time series were filtered at each carrier frequency used for the wavelet decomposition, i.e., 0.5 to 200 Hz. A narrow bandpass FIR filter was used centered at each carrier frequency and of width a fifth of the carrier frequency. Additionally, signals were mirror-padded prior to filtering to reduce ringing artefacts. Time delays related to pICM were extracted directly from the filtered signals, while the logarithm of the power envelope using Hilbert transform was used to extract time delays of envelope ICMs. Time delays were computed robustly by means of cross-correlation combined with a sliding window approach. A window of 5 s with 25% overlap was used to extract segments. For each segment, the normalized cross-correlation between each pair of areas is calculated. Subsequently, these cross-correlation function estimates were averaged across all sliding window segments within each session, and the estimated delay is given by the lag for which the averaged normalized cross-correlation has the largest absolute value. Maximum allowed lag was set to 500 ms. Time delay matrices were subsequently averaged within the canonical frequency bands, and across sessions and animals, as for the ICMs.

2.4. Structural connectivity

Ferret brain structural connectivity data were based on diffusion MRI tractography covering the 13 areas available from the micro-ECoG recordings (Delettre et al., 2019). High resolution MRI were acquired *ex vivo* from a 2 month old ferret using a small animal 7 Tesla Bruker MRI scanner (Neurospin, Saclay, France). The ferret was euthanized by an overdose of pentobarbital and perfused transcardially with 0.9% saline solution and post-fixed with phosphate-buffered 4% paraformaldehyde (PFA). After extraction, the brain was stored at 4 °C in a 4% PFA solution until the MRI acquisition. All procedures were approved by the Institutional Animal Care and Use Committee of the Universidad Miguel Hernández and the Consejo Superior de Investigaciones Científicas, Alicante, Spain.

High resolution T2-weighted MRI data was acquired using a multislice multiecho sequence with 18 echo times and 0.12 mm isotropic voxels. Diffusion MRI data were acquired using a multislice 2-D spin-echo segmented EPI sequence (4 segments) with the following parameters: TR = 40 s; TE = 32 ms; matrix size = 160×120×80; 0.24 mm isotropic voxels; 200 diffusion-weighted directions with b = 4000 s/mm^2; and 10 b0 at the beginning of the sequence, diffusion gradient duration = 5 ms and diffusion gradient separation = 17 ms. The total acquisition time of the diffusion MRI sequences was about 37 hr.

Diffusion MRI were first visually inspected to exclude volume with artefacts. Then, the following preprocessing steps were carried out: local principal component analysis denoising (Veraart et al., 2016), Gibbs ringing correction (Kellner et al., 2016), FSL-based eddy current correction (Andersson and Sotiropoulos, 2016; Jenkinson et al., 2012) and B1 field inhomogeneity correction (Tustison et al., 2010). A brain mask was manually segmented from the high-resolution T2 volume. Spatial normalization using a linear transformation between the high-resolution T2 volume and diffusion MRI data was computed using FLIRT tools (Jenkinson et al., 2002), and the brain mask was registered to the diffusion space. Tractography was performed based on the fiber orientation distribution estimated with a multishell multitissue constrained spherical deconvolution (msmt CSD) (Christiaens et al., 2015). Spherical harmonic order was set to 8. The response functions were computed using the 'dhollander' algorithm which provides an unsupervised estimation of tissue-specific response functions. The msmt CSD was performed using a WM/CSF compartment model (Jeurissen et al., 2014). The streamline tractographies were then produced following a probabilistic algorithm (iFOD2) (Tournier et al., 2012). One million streamlines were tracked over the full brain with the parameters recommended by MRtrix3: stepsize 0.12 mm, angle 45° per voxel, minimal streamline length 1.2 mm, maximal length 2.4 cm. Streamline seeds were produced at random locations within the brain mask until the defined number of streamlines was reached. To prevent streamlines from going across sulci, the brain mask was used as a stopping criterion.

A structural connectivity matrix was extracted from the tractography output using the number of streamlines connecting pairs of regions of a parcellation based on the atlas of the posterior cortex by Bizley and King (2009). The parcellation scheme was manually drawn on the left hemisphere in the diffusion MRI space using the online tool BrainBox (http://brainbox.pasteur.fr/). The structural connectivity matrix was inherently symmetric as diffusion MRI tractography does not provide any information about directionality. A matrix reporting the averaged fiber lengths between regions was also computed. The structural connectivity network is represented by the weighted matrix A, where the entries a_{ij} are the weights of the connections, i.e., the number of streamlines, between pairs of areas i and j.

All data analysis was performed using custom scripts for Python (http://www.python.org/) and the MRtrix3 software (http://www.mrtrix.org/).

2.5. Computational models

We employed computational models of various complexity: the spiking attractor network model, a biologically realistic model of a large network of spiking neurons (Deco and Jirsa, 2012), the Wilson-Cowan model, a popular neural-mass model of coupled excitatory and inhibitory populations (Wilson and Cowan, 1972), and the spatial autoregressive model, a statistical model capturing the stationary behavior of a diffuse process on networks (Messé et al., 2015a). All models incorporated a parameter that represents the coupling strength between regions. This parameter was optimized separately for each model, see Statistics section. The structural connectivity matrix was normalized before simulations such that the matrix's rows sum to one (Cabral et al., 2011; Messé et al., 2014; Tononi et al., 1994).

2.5.1. Spiking attractor network model

The SAN model is a detailed computational model based on spiking neurons and realistic synapses. A description for the microscopic level, that is within areas, is achieved by using a biologically realistic model of interconnected populations of excitatory and inhibitory neurons. The postsynaptic activity is dependent on the incoming synaptic input currents from other neurons through AMPA, NMDA and GABA receptors, as well as from external background input modeled by Poisson spike trains. Excitatory populations are interconnected at large-scale (inter-areal) *via* the structural connectivity scaled by a global coupling strength factor. For a detailed description of the model refer to Deco and Jirsa (2012), all parameter values (except the coupling strength) were retained from the original study.

We explored coupling parameter values from 0.1 to 10 by steps of 0.1. For each coupling strength value, the SAN model was simulated at a sampling frequency of 10 kHz for 5 min. The resulting data were then downsampled to 1 kHz. Simulated ICMs from the neuronal activity were extracted in a similar way as for the empirical data from a time-frequency decomposition of the simulated signals.

2.5.2. Wilson-Cowan model

The WC model represents a network of neural masses describing the activity of an ensemble of excitatory (E) and inhibitory (I) neuronal populations (Deco et al., 2009; Wilson and Cowan, 1972). The dynamics is governed by the following equations:

$$\tau_E \frac{\partial E_i(t)}{\partial t} = -E_i(t) + \phi\left(w_{ee} E_i(t) + w_{ie} I_i(t) + k \sum_j a_{ij} E_j\left(t - \tau_{ij}\right) + I_b + \sigma v_{Ei} \right)$$

$$\tau_I \frac{\partial I_i(t)}{\partial t} = -I_i(t) + \phi\left(w_{ei} E_i(t) + w_{ii} I_i(t) + \sigma v_{Ii} \right),$$

where E_i (resp. I_i) represents the average firing rate of the excitatory (resp. inhibitory) population i, and τ_E (resp. τ_I) the excitatory (resp. inhibitory) time constant. w_{ab} is the local connectivity strength between populations a and b, and k represents the global coupling strength. $A = \left\{a_{ij}\right\}$ represents the structural connectivity matrix. I_b is a constant spontaneous background input. τ_{ij} is the propagation delay between regions i and j, based on the average fiber tract length between regions scaled by the axonal velocity, v, i.e., $\tau_{ij} = L_{ij}/v$. v is a random fluctuating input accounting for sources of biophysical variability, scaled by σ. The transfer function ϕ accounts for the saturation of firing rates in neuronal populations and is modeled by a sigmoid: $\phi(x) = [1 + e^{-(x-a)/b}]^{-1}$. All parameter values (except the coupling strength and the delay) were set as in Abeysuriya et al. (2018).

We explored coupling strength values from 0.025 to 1 by steps of 0.025, and mean delay values from 0 to 50 ms by steps of 2 ms. For each pair of parameter values, the WC model was simulated at a sampling frequency of 10 kHz for 5 min. The resulting data were then downsampled to 1 kHz. As excitatory pyramidal cells contribute most strongly to EEG/MEG/ECoG signals, we associate activity in the excitatory populations of the model with signals in experimental data (Buzsáki et al., 2012). Simulated ICMs from the neuronal activity were then extracted in a similar way as for the empirical data from a time-frequency decomposition of the simulated signals.

2.5.3. Spatial autoregressive model

The SAR model assumes that fluctuating neuronal signals, $\mathbf{x} = \left\{x_i\right\}$, are related through a model of structural equations, which relies on expressing each signal as a linear function of the others and weighted by a global coupling factor k, leading to

$$\mathbf{x} = kA\mathbf{x} + \mathbf{e}. \tag{5}$$

A represents the structural connectivity matrix, $\mathbf{e}$ is some additive noise that stands for the part of the signal that cannot be accounted for by SC. It is usually assumed to be normally distributed with zero mean and unknown covariance Σ, with spatial and temporal independence. We here further assumed that the variance of $\mathbf{e}$ is uniform across areas, reducing its covariance to a single constant value, $\Sigma = \sigma^2$. Accordingly, $\mathbf{x}$ is multivariate normal with covariance

$$(I - kA)^{-1}\sigma^2(I - kA')^{-1}, \tag{6}$$

where I stands for the identity matrix, and $'$ is the regular matrix transposition. This model is also known as the simultaneous autoregressive model (Messé et al., 2015a), which has been extensively used for the analysis of spatial data from diverse disciplines such as demography, economy and geography (de Oliveira and Song, 2008; Lesage and Olivier, 2007).

We explored coupling parameter values from 0.001 to 0.999 by steps of 0.02. The SAR model provides a closed form for the covariance matrix that can be used to directly compute the predicted ICMs *via* its normalization. Of note, the SAR model does not provide frequency-resolved ICMs, we assume a common pattern across frequency bands.

2.5.4. Model optimization

To evaluate the predictive power of the different models, we computed the Spearman correlation as well as distance between simulated and empirical ICM matrices. The distance (D) between two matrices A and B is defined as the root-mean-square deviation, also known as the Frobenius norm,

$$D(A, B) = \sqrt{\sum_{i>j} (a_{ij} - b_{ij})^2}. \tag{7}$$

Optimal model parameters should maximize the similarity between simulated and empirical ICMs. This similarity was assessed using a simple objective function, representing the distance between simulations and empirical data:

$$Obj(ICM, F, \Omega) = D(ICM_{sim}(\Omega), ICM_{emp})\left[1 - corr(ICM_{sim}(\Omega), ICM_{emp})\right], \tag{8}$$

where F denoted the frequency band of interest, Ω the set of model's parameters, $ICM_{sim}(\Omega)$ the simulated ICM (either phase or envelope) according to the model's parameters Ω, and ICM_{emp} the corresponding empirical ICM measure. Optimal model parameters are those minimizing the sum of the objective functions averaged across all frequency bands:

$$\arg\min_{\Omega} \sum_{F} Obj(ICM, F, \Omega). \tag{9}$$

We explored different strategies of optimization by either minimizing the objective functions averaged over all ICM measures combining both original and lagged measures and time delays (one parameter set; *all*), over only original (*original*), only lagged (*lagged*) or only time delay (*delays*) ICMs (three parameter sets), or for each ICM measure individually (six parameter sets; *individual*).

2.6. Statistics

In order to probe the structure-function relationships, we computed the Spearman correlation between SC and phase and envelope ICM values for each frequency band, each animal and the group average. Additionally, we explored how much of the structure-function relationships may be explained by inter-areal distance, using the partial Spearman correlations. We also computed marginal Spearman correlations of both SC and ICMs with the distance. Similarity between phase and envelope ICMs was quantified by means of the Spearman correlation between the respective patterns for each frequency band, each animal and the group average. We computed also, for each type of ICM, the interfrequency consistency, i.e., the similarity between all pairs of frequency bands within each animal and the group average, and the interindividual consistency, i.e., the similarity between all pairs of animals within each frequency band. Since all brain connectivity measures are symmetrical, all correlation coefficients were computed using the upper triangular part of each connectivity matrix for the different scenarios.

In order to test the significance of the correlation coefficients or the significance of the difference between correlation coefficients (e.g., the correlation of pICMs with SC compared to the correlation of eICMs with SC), we used surrogate data based on the Fourier tranformation (Lancaster et al., 2018). Specifically, we used the amplitude-adjusted Fourier transform (AAFT) phase randomization (Lancaster et al., 2018; Theiler et al., 1992), which generate surrogate data by shuffling the phase spectra of the time series. AAFT preserves both the linear structure (i.e. the power spectral density and consequently the auto-correlation) and the amplitude distribution of the individual time series while destroying any potential interdependence between time series. For each animal and each period, we generated 200 surrogates at the area-level, applied the processing pipeline as designed for the original ECoG signal to extract the corresponding ICM measures (we therefore obtained 200 phase and envelope ICM surrogates, at each level), then, computed the structure-function relationships. To test the significance of the ICM time delays and their relationship with SC, we built a permutation-based null model by shuffling the windowed segments before calculating cross-correlation. For each animal and each session, we generated 200 surrogates at the area-level, applied the processing pipeline as designed for the original ECoG signal to extract the corresponding time delay ICM measures, then, computed the relationships with SC and distance. Consequently, we determined the probability (p) that the original (difference between) correlation coefficient values belong to the surrogate distributions, i.e. the null hypothesis. To compare the distributions of the time delays we used the two-sample Kolmogorov-Smirnov test. All statistical tests were rejected at $p < 0.05$ significance. Correction for multiple comparisons was performed by controlling the false discovery rate when appropriate (Benjamini et al., 2006).

3. Results

Intrinsic coupling modes were extracted from micro-ECoG data of ongoing brain activity from awake ferrets (Stitt et al., 2017). Cortical activity (local field potentials) was recorded in five adult female ferrets over multiple sessions using a 64 electrodes array distributed over half of the left posterior cortical hemisphere. The animals' brain states had been previously classified into slow-wave sleep, rapid-eye-movement sleep and awake periods using a data-driven approach (Stitt et al., 2017). The present study focused only on data from awake periods. Electrodes were first re-referenced and then assigned to cortical areas using the atlas of Bizley and King (2009), and the average signal for each area was computed (Fig. 1A and B). For each animal and each awake period, pICMs and eICMs were computed in a frequency resolved manner (0.5–200 Hz) between all pairs of areas by quantifying phase locking and power correlation, respectively, while time delays were computed using windowed cross-correlations. Subsequently, ICM matrices were averaged within data-driven frequency bands: 3–6 Hz (θ); 9–20 Hz (β_1); 20–35 Hz (β_2); and 55–145 Hz (γ) (Fig. 1B and Fig. S1). ICM matrices were averaged across awake periods within each session per animal (session-level), across sessions within each animal (animal-level), and also across animals (group-level). Results on the animal- and group-levels are presented in the main text, while results on the session-level are reported in supplementary figures. The corresponding structural connections of the areas covered by the micro-ECoG array were assembled from diffusion MRI tractography data (Delettre et al., 2019) (Fig. 1C). Finally, in order to predict empirical patterns of ICMs, we employed computational biophysical models of various complexity (Fig. 1D). See Material and Methods section for further details.

3.1. Structure-function relationships

The similarity between ICM patterns and the underlying structural connectivity was quantified, for each animal and the group average, and for each frequency band, by means of Spearman correlations between SC and phase and envelope ICM values. Envelope ICMs were significantly positively correlated to SC across all frequency bands, all animals and the group average. Phase ICMs were significantly positively correlated to SC across all frequency bands for the group average, all animals for the β_2 and γ bands, and four animals for the β_1 band (Fig. 2B). The correlations of phase and envelope ICMs with SC were not significantly different across frequency bands for all animals and the group average; we observed however consistently higher correlations of eICMs compared to pICMs with SC. Next, we evaluated the influence of the physical distance between areas in the structure-function relationships. As expected, both SC and ICMs were significantly negatively correlated with distance (except for pICMs for the θ band in two animals and for the β_1 band in one animal). Similar for both, connectivity values decrease with increasing inter-areal distance (Fig. 2B). Consequently, the correlation between SC and ICMs was reduced when controlling for distance, where the effect was more pronounced for pICMs. Phase ICMs were not significantly correlated to SC when controling for distance, except for two animals in the γ band, while envelope ICMs remained significantly correlated (Fig. 2B).

In addition, in order to deal with potential confounds resulting from volume conduction, we also computed the correlation between SC and lagged ICM measures (Fig. 2C). Envelope ICMs were significantly positively correlated to SC across all frequency bands, all animals and the group average. Phase ICMs were found to be only significantly positively correlated to SC in the γ band across all animals and the group average,

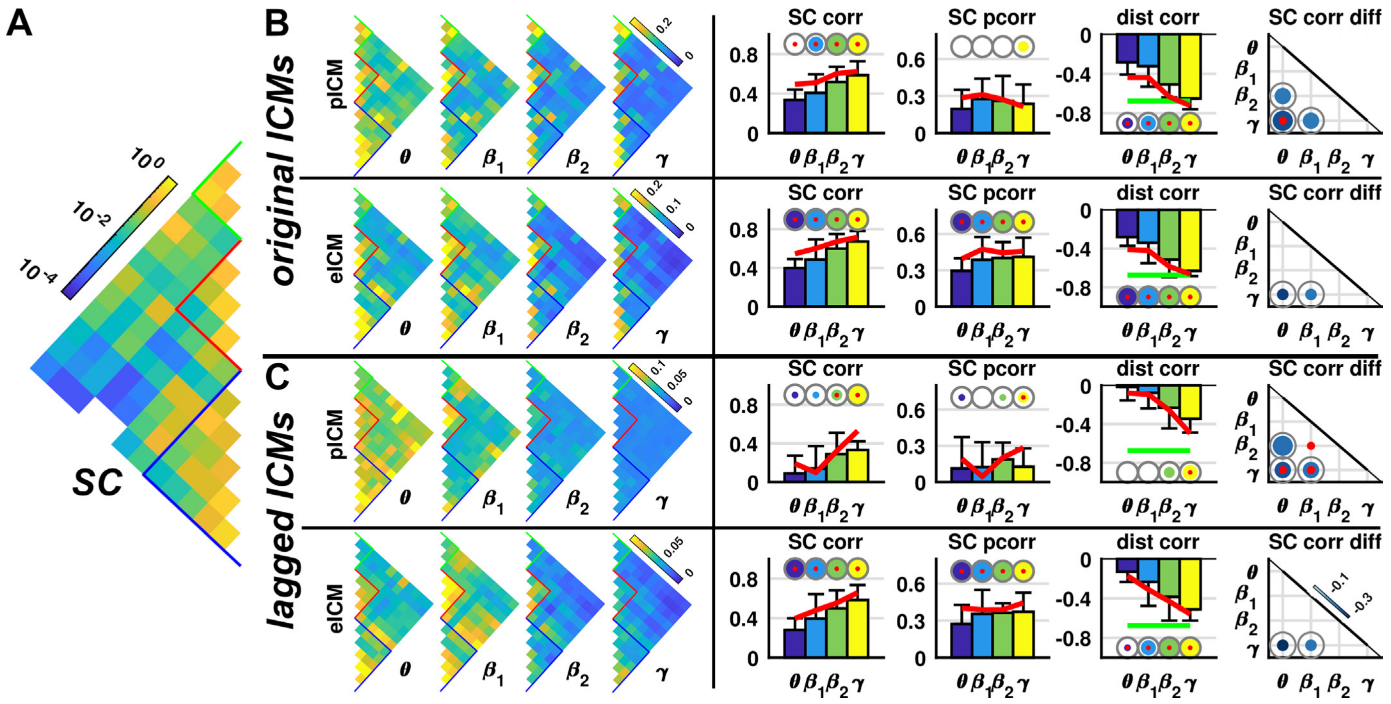

Fig. 2. Structure-function relationships. (A) Pattern of structural connectivity extracted from diffusion MRI tractography. (B) Correlation between structural connectivity and phase and envelope ICMs across frequency bands and animals. (Left) Patterns of group average phase and envelope ICMs across frequency bands. (Right) For each ICM measure and each frequency band, we represented the individual correlations (bar chart representing means and associated standard deviations), as well as the correlation for the group average (red curve), between SC and ICMs (SC corr), between SC and ICMs when controlling for the distance (SC pcorr), and between distance and ICMs (dist corr). The green line represents the correlation between distance and SC. Disks size within each subpanel represents the proportion of animals for whom there is a significant correlation (grey circles represent the maximum), red dots represent significant correlation for the group average ($p < 0.05$, FDR-corrected). The rightmost panels (SC corr diff) represent the differences in correlations between ICMs and SC between pairwise low versus high frequency bands. Disks size represents the proportion of animals for whom there is a significant difference in correlation (grey circles represent the maximum) and color represents the associated averaged difference ($p < 0.05$, FDR-corrected). (C) Same as (B) when using lagged ICM measures. (For interpretation of the references to colour in this figure legend, the reader is referred to the web version of this article.)

and in all frequency bands for one animal. One other animal had a significant positive correlation with SC in the β_2 band. The correlation of SC with pICMs was significantly lower compared to eICMs in most animals and frequency bands. Envelope ICMs were significantly negatively correlated with distance across all frequency bands except the θ band for 4 animals and the β_1 band for one animal (Fig. 2C). Phase ICMs were significantly negatively correlated with distance only for high frequency bands. The patterns of correlations between SC and lagged phase and envelope ICMs remained overall unchanged when controlling for distance (Fig. 2C).

For both the original and lagged ICM measures, we observed an increase in the correlation with SC with increasing frequency, where correlations appeared significantly lower when comparing pairwise low versus high frequency bands, especially comparing with the γ band. For the results at the level of individual animals see Fig. S2 and Fig. S3.

Taken together, the results show that both phase and envelope ICMs are related to SC, albeit with different strength, and that the relationship strengthens with increasing frequency. Using ICM measures insensitive to volume conduction diminishes the association, especially for pICMs. Brain spatial embedding largely influences connectivity patterns (both structural and functional), but cannot explain by itself the structure-function relationships. In order to better understand how both types of ICM are associated with SC, in the next section we explore in detail ICM similarity and consistency.

3.2. *ICM similarity and consistency*

The similarity between pICMs and eICMs was quantified, for each frequency band, each animal and the group average, by means of Spearman correlation. Phase and envelope ICMs were significantly positively correlated with each other in all frequency bands for all animals (Fig. 3A). Consistency of ICM measures across frequency bands was quantified, for each pair of frequency bands, each animal and the group average, by means of Spearman correlation. We observed a significant high interfrequency consistency for each ICM measure which was consistent across animals (Fig. 3A). Of note, the similarity was higher between ICM measures within frequency bands than across frequency bands for each ICM measure. We also assessed the consistency of both ICM measures across animals, for each pair of animals, and each frequency band, by means of Spearman correlation. Interindividual consistency was largely significant across animals for both ICM measures, but with moderate correlation values, except for the pICMs in the θ and β_1 bands (Fig. 3A).

When lagged ICM measures were used, consistent results were also observed, but correlation values were much lower (Fig. 3B). Phase and envelope ICMs were significantly positively correlated with each other for all frequency bands and animals, albeit at a lower level compared to the original ICM measures (Fig. 3B). Interfrequency consistency of lagged ICMs was significant across most animals and pairs of frequency bands, albeit at a much lower level compared to the original ICM measures (Fig. 3B). Interindividual consistency of eICMs was significant across all pairs of animals and all frequency bands, while it was virtually non significant for pICMs (Fig. 3B).

For both the original and lagged measures, we observed an increase in the interindividual consistency of phase and envelope ICMs with increasing frequency. For a more detailed presentation of the results at the level of individual animals see Fig. S4 and Fig. S5.

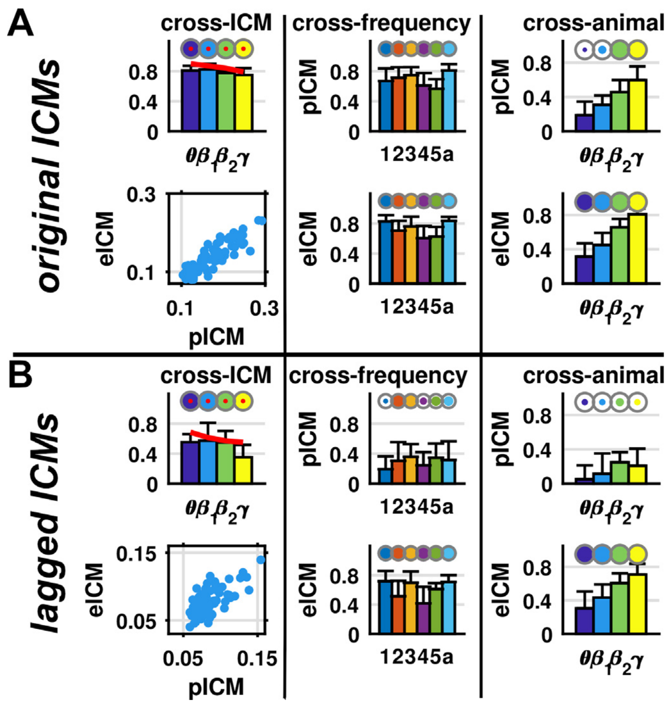

Fig. 3. ICM similarity and consistency. (A) Similarity of phase and envelope ICMs, and consistency across frequency bands and animals. (Left) Correlation between phase and envelope ICMs across frequency bands and animals. (Top) For each frequency band, we represented the individual correlations (bar chart representing means and associated standard deviations), as well as the correlation for the group average (red curve). (Bottom) Example scatter plot of phase versus envelope ICM values for the group average in the β_1 band. (Middle) Correlation of phase (top) and envelope (bottom) ICM patterns between frequency bands. For each ICM measure, each animal (1 to 5) and the group average (a), we represented all pairwise correlations between frequency bands (bar chart representing means and associated standard deviations). (Right) Correlation of phase (top) and envelope (bottom) ICM patterns between animals. For each ICM measure and each frequency band, we represented all pairwise correlations between animals (bar chart representing means and associated standard deviations). Disks size within each subpanel represents the proportion of correlations significant (grey circles represent the maximum), red dots represent significant correlation for the group average ($p < 0.05$, FDR-corrected). (B) Same as (A) when using lagged ICM measures. (For interpretation of the references to colour in this figure legend, the reader is referred to the web version of this article.)

Taken together, the results show that the original phase and envelope ICMs are largely similar to each other and consistent across frequencies. Using lagged ICM measures considerably diminishes the consistency across frequencies, especially for pICMs, but maintains a relatively high similarity between measures. These results support consistent structure-function relationship for both phase and envelope as observed in the previous section. Furthermore, ICM measures appear more consistent across animals with increasing frequency. To further support the perspective of a genuine structure-function relationship which is not solely due to experimental artifacts, especially volume conduction effects, in the next section we explore time delays.

3.3. Time delay ICMs

Phase (resp. envelope) time delay ICMs were computed, for each frequency band, each animal and the group average, by the lag at which the normalized cross-correlation of the signal (resp. envelope) had the largest absolute value. Time delay values appeared to drop for increasing frequency (Fig. 4). Time delay values were significantly lower than the ones from the surrogate data. Comparing phase and envelope time delay ICMs, we observed that eICM delays appeared more broadly distributed, and were significantly smaller than pICM delays for the θ and β_1 bands ($p < 0.05$, Kolmogorov-Smirnov test). Importantly, virtually all delays were different from zero.

Then, the similarity between time delay ICMs, the underlying structural connectivity and distance was quantified, for each animal and the group average, and for each frequency band, by means of Spearman correlations between connectivity values. Phase and envelope time delay ICMs were both significantly negatively correlated to SC across virtually all frequency bands, all animals and the group average; while they were both significantly positively correlated to distance (Fig. 4). The correlation between SC and ICMs time delays were reduced when controlling for distance; the effect was more pronounced for pCIMs where partial correlation values were only significant for high frequencies in few animals. Interestingly, similar to the structure-function relationship, the correlation between time delay ICMs and both SC and distance strengthens with increasing frequency. For a more detailed presentation of the results at the level of individual animals see Fig. S6.

Taken together, the results show that phase and envelope ICMs arise mostly from non-zero lag interactions. Consequently, the observed relationship between structural connectivity and ICMs cannot be solely attributed to volume conduction artifacts. Moreover, the decreasing delay with increasing frequency could explain the associated increasing structure-function relationship. Next, we explored the ability of classical computational models to predict such ICM patterns.

3.4. Computational modeling

We employed computational models at different levels of complexity for predicting ICM measures: (i) a microscopic description, the spiking attractor network (SAN) model, a biologically realistic model of a large network of spiking neurons; (ii) a mesoscopic model, the Wilson-Cowan (WC) model, a popular neural-mass model of coupled excitatory and inhibitory populations; and (iii) the spatial autoregressive (SAR) model, a statistical model capturing the macroscopic stationary behavior of a diffuse process on networks. We quantitatively fit the models using different optimization strategies to explore the models' ability to predict ICM measures (see Material and Methods section for details). Model parameters were chosen to minimize an objective function, defined as the distance between simulated and empirical ICMs averaged across frequency bands. We either minimized the objective function averaged across all ICM measures combining both original and lagged measures and time delays (one parameter set; *all*), over only original (*original*), only lagged (*lagged*) or only time delays (*delay*) ICMs (three parameter sets), or for each ICM measure individually (six parameter sets; *individual*).

Parameter space exploration highlights the sensitivity of the objective function to model parameter values, the global coupling strength and mean delay (Fig. S7). In general, optimal parameters settings (minimizing the distance between simulated and empirical ICMs) across the different strategies are located within the same area. Globally, computational models predicted phase and envelope ICMs in a very similar way (Fig. 5). All correlations between simulated and empirical ICMs were significantly positive, except for lagged ICM measures at low frequency. Even when specifically optimizing lagged ICM measures (*lagged* and *individual*), no model seemed to be able to predict these ICM patterns accurately, especially for pICMs. Moreover, time delay ICMs were generally poorly predicted by any model and strategy (of note, the SAR model was not considered as it does not include delays in its formalism). Simulated ICMs were not significantly more strongly correlated to the empirical data, when compared to the respective correlations with SC, except for the original envelope ICMs and to some extent the lagged envelope ICMs (Fig. S8).

Overall, these results highlight the challenge of properly fitting biophysical models to rich empirical datasets. The overall predictive ability of these models appears to rely moslty on the general association between the underlying SC with the empirical ICMs.

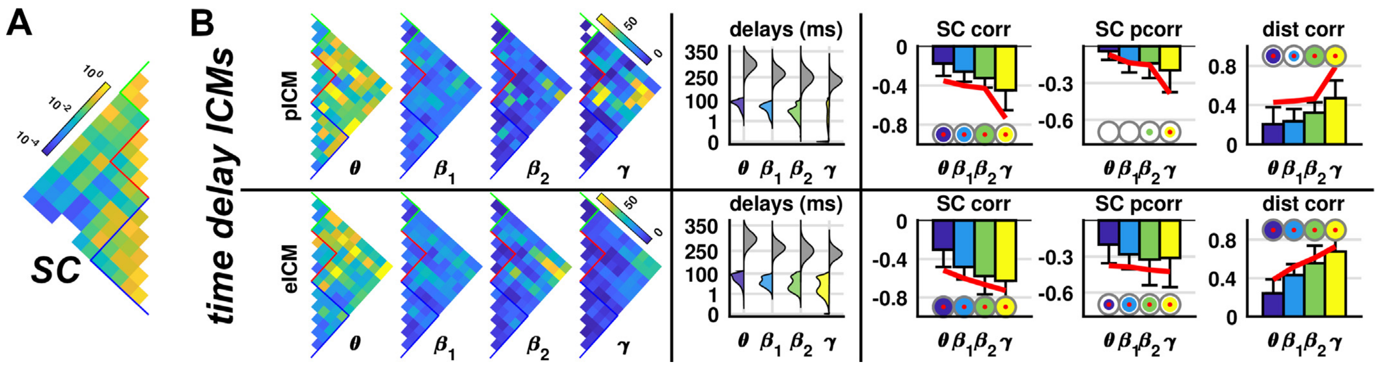

Fig. 4. Time delay ICMs. (A) Pattern of structural connectivity extracted from diffusion MRI tractography. (B) Correlation between structural connectivity and phase and envelope time delay ICMs across frequency bands and animals. (Left) Patterns of group average phase and envelope time delay ICMs across frequency bands. (Middle) Distribution of time delays extracted for phase and envelope ICMs and the corresponding surrogates (gray). (Left) For each ICM measure and each frequency band, we represented the individual correlations (bar chart representing means and associated standard deviations), as well as the correlation for the group average (red curve), between SC and time delay ICMs (SC corr), between SC and time delay ICMs when controlling for the distance (SC pcorr), and between distance and time delay ICMs (dist corr). Disks size within each subpanel represents the proportion of animals for whom there is a significant correlation (grey circles represent the maximum), red dots represent significant correlations for the group average ($p < 0.05$, FDR-corrected). (For interpretation of the references to colour in this figure legend, the reader is referred to the web version of this article.)

4. Discussion

4.1. Overview

In the present study, we investigated the relationship between structural connectivity and ICMs of ongoing dynamics in the ferret brain. We took advantage of the high temporal resolution offered by micro-ECoG measurements to explore these relationships across multiple frequency bands and different animals. We also investigated the similarity between phase and envelope ICMs across frequency bands, as well as their inter-frequency and interindividual consistency. Additionally, we computed the time delays at which ICMs occur. Finally, we explored and compared the performance of computational models of various complexity in predicting simultaneously envelope and phase ICMs. All investigations were conducted with classical ICM measures as well as with lagged measures insensitive to volume conduction effects. Generally, we found that SC was significantly related to both phase and envelope ICMs, but to different degrees. When using original ICM measures both pICMs and eICMs were largely similar and consistent across frequency bands and animals. However, using lagged ICM measures virtually abolished the association of pICMs with SC, except for high frequency, and reduced their consistency and similarity with eICM. Importantly, ICMs that occur at non-zero lag discard explanations purely due to volume conduction. Computational models are challenged to predict these ICM patterns consistently and simultaneously. The models are generally good at predicting original ICM measures, but fail for the lagged ones, especially at low frequency. Overall, our results suggest that ICMs during ongoing activity in awake ferrets reflect, to a significant degree, the organization of anatomical cortical networks, but are likely also influenced by further factors.

4.2. Structure-function relationships

In previous studies, envelope ICMs and their association with structural connectivity were mainly investigated using resting-state fMRI data, where consistent positive correlations were reported (Greicius et al., 2009; Hagmann et al., 2008; Koch et al., 2002; Messé, 2020; Messé et al., 2014; Vincent et al., 2007), reviewed in (Straathof et al., 2019). Some recent studies have extended and confirmed these observations based on the refined temporal resolution offered by electrophysiological measurements. The relationship between pICMs and SC has been explored using both EEG (Chu et al., 2015; Finger et al., 2016; Wirsich et al., 2017) and MEG (Meier et al., 2016; Tewarie et al., 2014) data, while eICMs were investigated using MEG recordings (Garcés et al., 2016; Tewarie et al., 2019). Similar to the resting-state literature, a positive relationship between both types of ICMs with SC has been reported consistently, but its potential frequency dependence has not been thoroughly investigated (Chu et al., 2015; Garcés et al., 2016). Here, we confirm these observations by showing that both types of ICMs are positively correlated with SC, with correlations increasing with increasing frequency. As a matter of fact, both measures also appeared to be correlated to each other independently of the frequency. Additionally, we observed a relatively high consistency of the original ICM measures both across frequencies and animals, similar to observations in MEG recordings (Colclough et al., 2016).

One important confound in the analysis of functional connectivity using electrophysiological measurements is the potential presence of signal mixing due to volume conduction. A number of measures and procedures have been designed to mitigate such effects. Most of them specifically remove zero-lag synchronization or coactivations (Bastos and Schoffelen, 2016). Nonetheless, reliable estimation of ICMs with electrophysiological recordings remains challenging due to signal mixing (Palva et al., 2018; Siems and Siegel, 2020). We observed that the similarity between phase and envelope ICMs, their consistency across frequencies and animals are largely abolished when using lagged measures, as previously reported (Colclough et al., 2016; Galindo-Leon et al., 2019), especially for pICMs. The correlation of pICMs with SC appears also largely reduced and virtually abolished, except for high frequency, compared to the original measures, while the correlation of eICMs with SC was reduced, but remained essentially unchanged. These results suggest that the classical phase ICM measures might be strongly driven by near-zero coactivations, which are in part resulting from volume conduction, but are in part also due to physiological synchrony (Engel et al., 2013; Fries, 2005; Uhlhaas and Singer, 2012), which occurs most prominently across short distances and depends on the underlying network structure (Messé et al., 2018).

To verify this explanation, we also extracted the corresponding time delays of phase and envelope ICMs. The results showed that both phase and envelope ICMs essentially occur at non-zero delays, and thus discard the possibility that the structure-function relationship is largely driven by volume conduction. In addition, the time delay values appeared to drop for increasing frequency bands, which coincides with the increased structure-function association. These observations agree with the finding (Vezoli et al., 2021) that ICMs derived by micro-ECoG

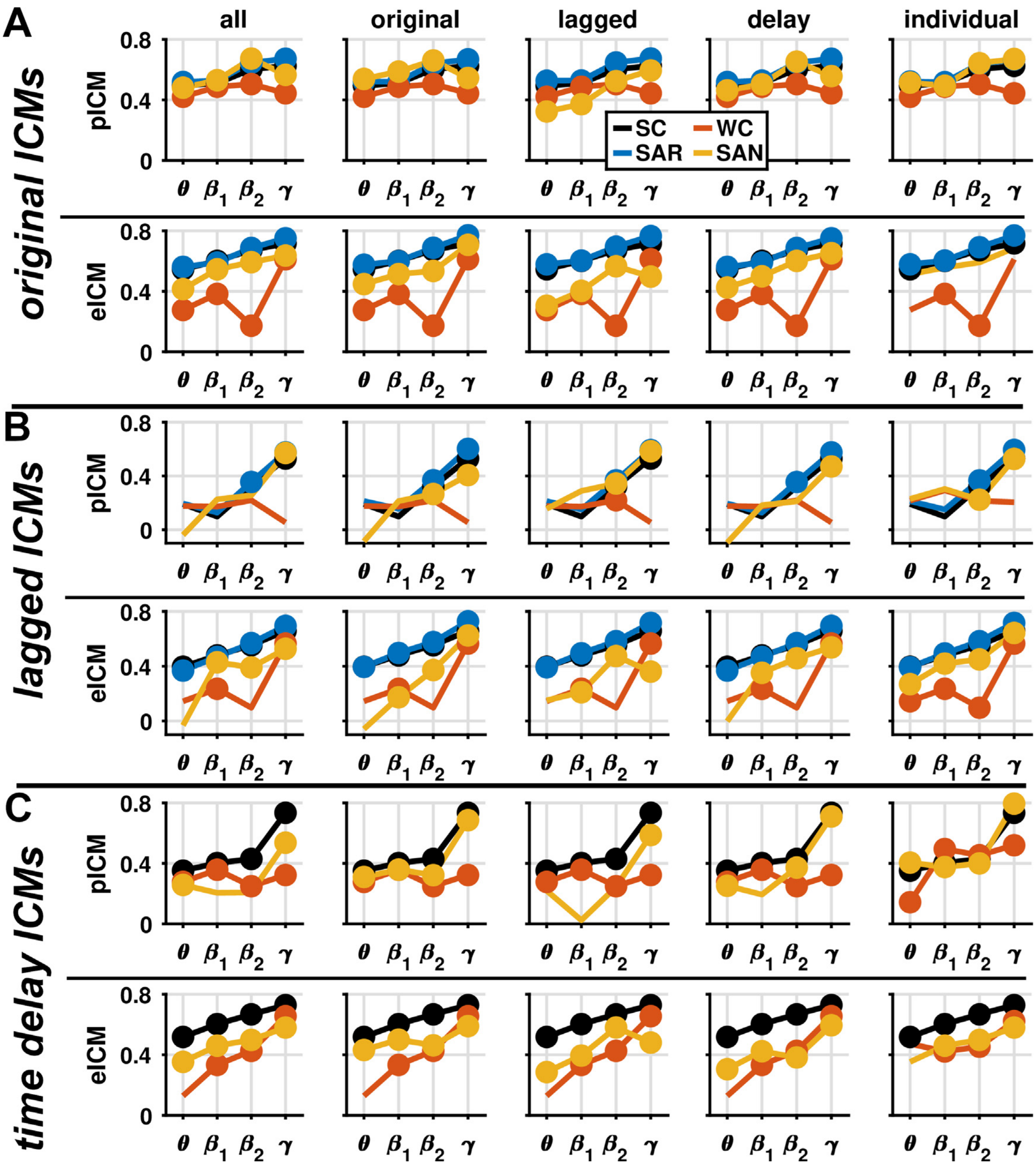

Fig. 5. Predictive power of the computational models. (A) Correlation between simulated and empirical phase and envelope ICMs across frequency bands and models when using original ICM measures. Columns represent the different optimization strategies. We either minimized the objective function averaged across all ICM measures combining both original, lagged and time delay measures (first column, *all*), over only original (second column, *original*), only lagged (third column, *lagged*) or only time delay (fourth column, *delay*) ICM measures, or for each ICM measure individually (last column, *individual*). Circles represent significant correlations ($p < 0.05$, FDR-corrected). (B, resp. C) Same as (A) when using lagged (resp. time delay) ICMs. Of note, we took the absolute value of the correlation between time delay ICMs and SC for visual comparison.

recordings in the macaque cerebral cortex also more closely align with structural connectivity for higher frequencies (γ) than lower frequencies (β). Interestingly, theoretical work has demonstrated a structure-function discrepancy in the presence of heterogeneous delays between neuronal populations (Ton et al., 2014).

4.3. ICMs models

Computational brain models provide a parsimonious approach to explore the generative mechanisms of ICMs (Breakspear, 2017; Cabral et al., 2014a; 2017). Most modeling studies have investigated the emergence of envelope ICMs using resting-state fMRI (Deco et al., 2011; Honey et al., 2009; Messé et al., 2014; 2015b) or MEG data (Abeysuriya et al., 2018; Cabral et al., 2014b; Tewarie et al., 2019), while few studies have explored the generative processes of phase ICMs using MEG (Abeysuriya et al., 2018) or EEG (Finger et al., 2016) recordings. Using computational models of various scales of complexity, we showed their potential for predicting both types of ICMs. None of the models investigated here appears to be able to predict simultaneously original and lagged ICM measures. As a matter of fact, no model could predict lagged measures, even when fitting the models explicitly to these measures, especially for phase ICMs. This finding is corroborated by the poor predictive ability of the models with regard to the time delays. Indeed, lagged measures are by definition dependent on delays as they explicitely consider non-zero lags (Nolte et al., 2004). One of the most intriguing results is the fact that none of the models seems to predict ICM patterns much better than SC by itself, except for envelope ICMs. As observed here, and as previously shown in resting-state fMRI studies, patterns of functional interactions appear significantly constrained by the underlying topological scaffold of the brain (Goñi et al., 2014; Marrelec et al., 2016; Messé et al., 2015b).

4.4. Biological significance

On the one hand, the removal of zero-lag interactions avoids artefacts that are known to arise from signal mixing at sensor level (Brookes et al., 2012; Hipp et al., 2012; Nolte et al., 2004). On the other hand, such a treatment may also remove actual physiological coupling. Indeed, the present results confirm that near zero-lag interactions are an essential component of cortical coupling modes (Engel et al., 2013; Fries, 2005; Siegel et al., 2012; Uhlhaas and Singer, 2012). Moreover, despite debates about the origin and spatial extent of cortical signals, as recorded with micro-ECoG approaches, recent investigations appear to point to a very local specificity (Dubey and Ray, 2019; Einevoll et al., 2013; Liu et al., 2015), comforting the idea that volume conduction is reduced in such experimental setup. Adjacent regions of the ferret cortex are strongly connected by short fibres (Delettre et al., 2019). This kind of connectivity supports very fast, near zero-lag interactions between neighbouring regions (Engel et al., 2001). The importance of these interactions for intrinsic cortical coupling is demonstrated by the observation that original ICMs strongly depend on the physical embedding in the cortex and decay with distance (Fig. 2B). Conversely, the dominant role of direct, short-distance interactions is abolished for lagged phase ICMs (Fig. 2C). We further support the role of short-distance interactions by looking at the structure-function correlation across distance bins (low, medium and long range distances), where we observed a general drop in correlation when distance increases (Fig. S9). Moreover, as structural cortical connectivity is dominated by short connections, the predictive power of computational models is much reduced for lagged versus original ICM measures. These findings once again underline the role of direct structural connectivity in cortical communication.

4.5. Caveats

The present results are subject to several methodological limitations. First, the spatial coverage of the micro-ECoG array was limited to roughly one half of a cerebral hemisphere which limits us for a potential generalization and prevents us to study, for example, interhemispheric structure-function relations which have been addresses in other preparations before (Engel et al., 1991) but shown to be challenging (Messé et al., 2014). Additionally, we solely focused on the awake resting-state periods in order to make concrete comparisons with the existing literature mostly based on resting state. Little is known about the modulation of the structure-function relationships across diverse contexts, including, for example, sleep stages or when animals interact with the environment, deserving further investigations (Galindo-Leon et al., 2019; Sjøgård et al., 2020). The study could have benefited also from the use of an inverse ECoG model to better map the cortical sources (Pesaran et al., 2018). Unfortunately, this approach requires the use of a proper ferret brain model which is not available yet. In terms of volume conduction, we mainly focused on first-order effects due to signal mixing, creating false positive connectivity at zero lag. However, other spurious interactions may arise from second-order effects, characterized by false positive connectivity caused by mislocalization of the “true” interacting sources (Palva et al., 2018). But, these second-order effects are very challenging to estimate and remove (Wang et al., 2018). Regarding computational modeling, we made use of standard models together with their default settings, except for the coupling strength and the average delay. For further refinement, one should consider to optimize a larger number of parameters or even to incorporate knowledge from external modalities including, for example, receptor maps (Deco et al., 2018) or anatomical laminar details (Schmidt et al., 2018), as in Mejias et al. (2016).

5. Conclusions

Our results derived from large-scale cortical recordings at high temporal and spatial resolution demonstrate that intrinsic cortical communication based on envelope as well as phase coupling is shaped, to a substantial degree, by the structural scaffold of cortical connections. It remains a challenge for future research to refine these relations and develop generally applicable computational models that can fully account for them.

Supporting information

Fig S1 **Power spectrum and oscillatory modes.** (A) Power spectral density estimated across animals and areas (averaged across awake periods and sessions). (B) Distribution of the oscillatory peaks detected over the 1/f trend across areas and all awake periods of all animals.

Fig S2 **Structure-function relationships across animals when using original ICM measures.** (A) Correlation between structural connectivity and phase and envelope ICMs across frequency bands, animals, and sessions when using original ICM measures. For each ICM measure, each animal and each frequency band, we represented the individual session correlations (bar chart representing means and associated standard deviations), as well as the correlation for the average session (red curve), between SC and ICMs (SC corr). (B) Same as (A) when controlling for the distance (SC pcorr). (C) Same as (A) when correlating ICMs with distance (dist corr). The green line represents the correlation between distance and SC. Disks size within each subpanel represents the proportion of sessions for whom there is a significant correlation (grey circles represent the maximum), red dots represent significant correlation for the corresponding animal ($p < 0.05$, FDR-corrected). (D) Differences in correlations between ICMs and SC between pairwise low versus high frequency bands (SC corr diff). Disks size represents the proportion of sessions for whom there is a significant difference in correlation and color represents the associated averaged difference ($p < 0.05$, FDR-corrected).

Fig S3 **Structure-function relationships across animals when using lagged ICM measures.** (A) Correlation between structural connectivity and phase and envelope ICMs across frequency bands, animals, and sessions when using lagged ICM measures. For each ICM measure, each animal and each frequency band, we represented the individual session correlations (bar chart representing means and associated standard deviations), as well as the correlation for the average session (red curve), between SC and ICMs (SC corr). (B) Same as (A) when controlling for the distance (SC pcorr). (C) Same as (A) when correlating ICMs with distance (dist corr). The green line represents the correlation between distance and SC. Disks size within each subpanel represents the proportion of sessions for whom there is a significant correlation (grey circles represent the maximum), red dots represent significant correlation for the corresponding animal ($p < 0.05$, FDR-corrected). (D) Differences in correlations between ICMs and SC between pairwise low versus high frequency bands (SC corr diff). Disks size represents the proportion of sessions for whom there is a significant difference in correlation and color represents the associated averaged difference ($p < 0.05$, FDR-corrected).

Fig S4 **ICM similarity and consistency across animals when using original ICM measures.** (A) Correlation between phase and envelope ICMs. For each animal and each frequency band, we represented the individual session correlations (bar chart representing means and associated standard deviations), as well as the correlation for the average session (red curve). (B) Interfrequency consistency of ICM patterns. For each animal, each ICM measure, and each session, we represented all pairwise correlations between frequency bands (bar chart representing means and associated standard deviations). (C) Intraindividual consistency of ICMs measures. For each animal, each ICM measure and each frequency band, we represented all pairwise correlations between sessions (bar chart representing means and associated standard deviations). Disks size within each subpanel represents the proportion of significant correlations (grey circles represent the maximum), red dots represent significant correlation for the corresponding animal ($p < 0.05$, FDR-corrected).

Fig S5 **ICM similarity and consistency across animals when using lagged ICM measures.** (A) Correlation between phase and envelope ICMs. For each animal and each frequency band, we represented the individual session correlations (bar chart representing means and associated standard deviations), as well as the correlation for the average session (red curve). (B) Interfrequency consistency of ICM patterns. For each animal, each ICM measure, and each session, we represented all pairwise correlations between frequency bands (bar chart representing means and associated standard deviations). (C) Intraindividual consistency of ICMs measures. For each animal, each ICM measure and each frequency band, we represented all pairwise correlations between sessions (bar chart representing means and associated standard deviations). Disks size within each subpanel represents the proportion of significant correlations (grey circles represent the maximum), red dots represent significant correlation for the corresponding animal ($p < 0.05$, FDR-corrected).

Fig S6 **Time delay ICMs across animals.** (A) Distribution of time delays extracted for phase and envelope ICMs and the corresponding surrogates (gray). (B) Correlation between structural connectivity and phase and envelope time delay ICMs across frequency bands, animals, and sessions. For each ICM measure, each animal and each frequency band, we represented the individual session correlations (bar chart representing means and associated standard deviations), as well as the correlation for the average session (red curve), between SC and time delay ICMs (SC corr). (C) Same as (B) when controlling for the distance (SC pcorr). (D) Same as (B) when correlating time delay ICMs with distance (dist corr). Disks size within each subpanel represents the proportion of sessions for whom there is a significant correlation (grey circles represent the maximum), red dots represent significant correlation for the corresponding animal ($p < 0.05$, FDR-corrected).

Fig S7 **Parameter space exploration of the computational models.** (A) Objective function as a function of the models' parameters when using original ICM measures. Columns represent the different models (left: SAR; middle: WC; and right: SAN). Parameter values were chosen to either minimized the objective function averaged across all ICM measures combining both original, lagged and time delay ICMs (blue circle, *all*), over only original (red diamond, *original*), only lagged (yellow square, *lagged*) or only time delay (purple star, *delay*) ICMs, or for each ICM measure individually (green hexagram, *individual*). (B, resp. C) Same as (A) when using lagged (resp. time delay) ICMs.

Fig S8 **Comparison of the predictive power of the computational models.** (A) Significance of the difference between models in the correlation between simulated and empirical original ICMs across frequency bands. For each frequency band, each ICM measure, and each optimization strategy (columns), we represented the significance of the difference between all pairs of models (including SC) in the correlation between simulated and empirical ICM measures. (B, resp. C) Same as (A) when using lagged (resp. time delay) ICMs.

Fig S9 **Structure-function relationships as a function of the distance.** Correlation between structural connectivity and phase and envelope ICMs across frequency bands and animals. For each ICM measure and each frequency band, we represented the individual correlations (bar chart representing means and associated standard deviations), as well as the correlation for the group average (red curve), between SC and ICMs according to different distance bins (columns). Disks size within each subpanel represents the proportion of animals for whom there is a significant correlation (grey circles represent the maximum), red dots represent significant correlation for the group average ($p < 0.05$, FDR-corrected). (B) Same as (A) when using lagged ICM measures.

Declaration of Competing Interest

None

Credit authorship contribution statement

Arnaud Messé: Conceptualization, Methodology, Software, Formal analysis, Writing – original draft, Writing – review & editing, Visualization. **Karl J. Hollensteiner:** Investigation, Resources. **Céline Delettre:** Formal analysis. **Leigh-Anne Dell-Brown:** Writing – review & editing. **Florian Pieper:** Investigation, Resources. **Lena J. Nentwig:** Writing – review & editing. **Edgar E. Galindo-Leon:** Investigation, Resources. **Benoît Larrat:** Resources. **Sébastien Mériaux:** Resources. **Jean-François Mangin:** Resources. **Isabel Reillo:** Resources. **Camino de Juan Romero:** Resources. **Víctor Borrell:** Resources. **Gerhard Engler:** Investigation, Resources. **Roberto Toro:** Resources, Funding acquisition. **Andreas K. Engel:** Supervision, Funding acquisition, Writing – review & editing. **Claus C. Hilgetag:** Supervision, Funding acquisition, Writing – review & editing.

Data availability

Data will be made available on request.

Acknowledgments

This work was supported by funding from the Deutsche Forschungsgemeinschaft (DFG, German Research Foundation) - SFB 936 - 178316478 - A1 (C.C.H.), A2 (A.K.E.), and Z3 (C.C.H. and A.M.), SPP1665 - 220176618 - EN533/13-1 (A.K.E.), SPP2041 - 313856816 - HI1286/6-1 (C.C.H.) and EN533/15-1 (A.K.E.), from the European Unions Horizon 2020 Framework Programme for Research and Innovation under Specific Grant Agreements 785907 and 945539 (Human Brain Project SGA2 and SGA3, C.C.H.), and from the 2015 FLAG-ERA Joint Transnational Call for project FIIND - ANR-15-HBPR-0005 (R.T.). The funders had no role in study design, data collection and analysis, decision to publish, or preparation of the manuscript. Declarations of interest: none.

Supplementary material

Supplementary material associated with this article can be found, in the online version, at 10.1016/j.neuroimage.2023.120212.

References

Abeysuriya, R.G., Hadida, J., Sotiropoulos, S.N., Jbabdi, S., Becker, R., Hunt, B.A., Brookes, M.J., Woolrich, M.W., 2018. A biophysical model of dynamic balancing of excitation and inhibition in fast oscillatory large-scale networks. PLoS Comput. Biol. 14, 1–27. doi:10.1371/journal.pcbi.1006007.

Andersson, J.L., Sotiropoulos, S.N., 2016. An integrated approach to correction for off-resonance effects and subject movement in diffusion mr imaging. Neuroimage 125, 1063–1078. doi:10.1016/j.neuroimage.2015.10.019.

Bastos, A.M., Schoffelen, J.M., 2016. A tutorial review of functional connectivity analysis methods and their interpretational pitfalls. Front. Syst. Neurosci. 9, 175. doi:10.3389/fnsys.2015.00175.

Benjamini, Y., Krieger, A.M., Yekutieli, D., 2006. Adaptive linear step-up procedures that control the false discovery rate. Biometrika 93, 491–507. doi:10.1093/biomet/93.3.491.

Bizley, J.K., King, A.J., 2009. Visual influences on ferret auditory cortex. Hear. Res. 258, 55–63. doi:10.1016/j.heares.2009.06.017.

Breakspear, M., 2017. Dynamics models of large-scale brain activity. Nat. Neurosci. 20, 340–352. doi:10.1038/nn.4497.

Brookes, M., Woolrich, M., Barnes, G., 2012. Measuring functional connectivity in MEG: a multivariate approach insensitive to linear source leakage. Neuroimage 63, 910–920. doi:10.1016/j.neuroimage.2012.03.048.

Brookes, M.J., Woolrich, M., Luckhoo, H., Price, D., Hale, J.R., Stephenson, M.C., Barnes, G.R., Smith, S.M., Morris, P.G., 2011. Investigating the electrophysiological basis of resting state networks using magnetoencephalography. Proc. Natl. Acad. Sci. U.S.A. 108, 16783–16788. doi:10.1073/pnas.1112685108.

Buzsáki, G., Anastassiou, C.A., Koch, C., 2012. The origin of extracellular fields and currents – EEG, ECoG, LFP and spikes. Nat. Rev. Neurosci. 13, 407–420. doi:10.1038/nrn3241.

Cabral, J., Hugues, E., Sporns, O., Deco, G., 2011. Role of local network oscillations in resting-state functional connectivity. Neuroimage 57, 130–139. doi:10.1016/j.neuroimage.2011.04.010.

Cabral, J., Kringelbach, M.L., Deco, G., 2014. Exploring the network dynamics underlying brain activity at rest. Prog. Neurobiol. 114, 102–131. doi:10.1016/j.pneurobio.2013.12.005.

Cabral, J., Kringelbach, M.L., Deco, G., 2017. Functional connectivity dynamically evolves on multiple time-scales over a static structural connectome: models and mechanisms. Neuroimage 160, 84–96. doi:10.1016/j.neuroimage.2017.03.045.

Cabral, J., Luckhoo, H., Woolrich, M., Joensson, M., Mohseni, H., Baker, A., Kringelbach, M.L., Deco, G., 2014. Exploring mechanisms of spontaneous functional connectivity in MEG: how delayed network interactions lead to structured amplitude envelopes of band-pass filtered oscillations. Neuroimage 90, 423–435. doi:10.1016/j.neuroimage.2013.11.047.

Christiaens, D., Reisert, M., Dhollander, T., Sunaert, S., Suetens, P., Maes, F., 2015. Global tractography of multi-shell diffusion-weighted imaging data using a multi-tissue model. Neuroimage 123, 89–101. doi:10.1016/j.neuroimage.2015.08.008.

Chu, C., Tanaka, N., Diaz, J., Edlow, B., Wu, O., Hämäläinen, M., Stufflebeam, S., Cash, S., Kramer, M., 2015. EEG functional connectivity is partially predicted by underlying white matter connectivity. Neuroimage 108, 23–33. doi:10.1016/j.neuroimage.2014.12.033.

Colclough, G., Woolrich, M., Tewarie, P., Brookes, M., Quinn, A., Smith, S., 2016. How reliable are meg resting-state connectivity metrics? Neuroimage 138, 284–293. doi:10.1016/j.neuroimage.2016.05.070.

Deco, G., Cruzat, J., Cabral, J., Knudsen, G.M., Carhart-Harris, R.L., Whybrow, P.C., Logothetis, N.K., Kringelbach, M.L., 2018. Whole-brain multimodal neuroimaging model using serotonin receptor maps explains non-linear functional effects of LSD. Curr. Biol. 28, 3065–3074. doi:10.1016/j.cub.2018.07.083.

Deco, G., Jirsa, V., McIntosh, A., 2011. Emerging concepts for the dynamical organization of resting-state activity in the brain. Nat. Rev. Neurosci. 12, 43–56. doi:10.1038/nrn2961.

Deco, G., Jirsa, V., McIntosh, A.R., Sporns, O., Kotter, R., 2009. Key role of coupling, delay, and noise in resting brain fluctuations. Proc. Natl. Acad. Sci. U.S.A. 106, 10302–10307. doi:10.1073/pnas.0901831106.

Deco, G., Jirsa, V., Robinson, P.A., Breakspear, M., Friston, K., 2008. The dynamic brain: from spiking neurons to neural masses and cortical fields. PLoS Comput. Biol. 4, e1000092. doi:10.1371/journal.pcbi.1000092.

Deco, G., Jirsa, V.K., 2012. Ongoing cortical activity at rest: criticality, multistability, and ghost attractors. J. Neurosci. 32, 3366–3375. doi:10.1523/JNEUROSCI.2523-11.2012.

Delettre, C., Messé, A., Dell, L.-A., Foubet, O., Heuer, K., Larrat, B., Mériaux, S., Mangin, J.-F., Reillo, I., de Juan Romero, C., Borrell, V., Toro, R., Hilgetag, C.C., 2019. Comparison between diffusion MRI tractography and histological tract-tracing of cortico-cortical structural connectivity in the ferret brain. Netw. Neurosci. 3, 1038–1050. doi:10.1162/netn_a_00098.

de Oliveira, V., Song, J.J., 2008. Bayesian analysis of simultaneous autoregressive models. Sankhya Indian J. Stat. 70, 323–350.

Donoghue, T., Haller, M., Peterson, E.J., Varma, P., Sebastian, P., Gao, R., Noto, T., Lara, A.H., Wallis, J.D., Knight, R.T., et al., 2020. Parameterizing neural power spectra into periodic and aperiodic components. Nat. Neurosci. 23, 1655–1665. doi:10.1038/s41593-020-00744-x.

Dubey, A., Ray, S., 2019. Cortical electrocorticogram (ECoG) is a local signal. J. Neurosci. 39, 4299–4311. doi:10.1523/JNEUROSCI.2917-18.2019.

Einevoll, G.T., Kayser, C., Logothetis, N.K., Panzeri, S., 2013. Modelling and analysis of local field potentials for studying the function of cortical circuits. Nat. Rev. Neurosci. 14, 770–785. doi:10.1038/nrn3599.

Engel, A., Konig, P., Kreiter, A., Singer, W., 1991. Interhemispheric synchronization of oscillatory neuronal responses in cat visual cortex. Science 252, 1177–1179. doi:10.1126/science.252.5009.1177.

Engel, A.K., Fries, P., Singer, W., 2001. Dynamic predictions: oscillations and synchrony in top-down processing. Nat. Rev. Neurosci. 2, 704–716. doi:10.1038/35094565.

Engel, A.K., Gerloff, C., Hilgetag, C.C., Nolte, G., 2013. Intrinsic coupling modes: multiscale interactions in ongoing brain activity. Neuron 80, 867–886. doi:10.1016/j.neuron.2013.09.038.

Finger, H., Bönstrup, M., Cheng, B., Messé, A., Hilgetag, C., Thomalla, G., Gerloff, C., König, P., 2016. Modeling of large-scale functional brain networks based on structural connectivity from DTI: comparison with EEG derived phase coupling networks and evaluation of alternative methods along the modeling path. PLoS Comput. Biol. 12, e1005025. doi:10.1371/journal.pcbi.1005025.

Fornito, A., Bullmore, E.T., 2015. Connectomics: a new paradigm for understanding brain disease. Eur. Neuropsychopharmacol. 25, 733–748. doi:10.1016/j.euroneuro.2014.02.011.

Foster, B.L., He, B.J., Honey, C.J., Jerbi, K., Maier, A., Saalmann, Y.B., 2016. Spontaneous neural dynamics and multi-scale network organization. Front. Syst. Neurosci. 10, 7. doi:10.3389/fnsys.2016.00007.

Fox, M., Raichle, M.E., 2007. Spontaneous fluctuations in brain activity observed with functional magnetic resonance imaging. Nat. Rev. Neurosci. 8, 700–711. doi:10.1038/nrn2201.

Fries, P., 2005. A mechanism for cognitive dynamics: neuronal communication through neuronal coherence. Trends Cogn. Sci. 9, 474–480. doi:10.1016/j.tics.2005.08.011.

Galindo-Leon, E.E., Stitt, I., Pieper, F., Stieglitz, T., Engler, G., Engel, A.K., 2019. Context-specific modulation of intrinsic coupling modes shapes multisensory processing. Sci. Adv. 5, eaar7633. doi:10.1126/sciadv.aar7633.

Garcés, P., Pereda, E., Hernàndez-Tamames, J.A., Del-Pozo, F., Maestù, F., Pineda-Pardo, J.A., 2016. Multimodal description of whole brain connectivity: a comparison of resting state MEG, fMRI, and DWI. Hum. Brain Mapp. 37, 20–34. doi:10.1002/hbm.22995.

Goñi, J., van den Heuvel, M.P., Avena-Koenigsberger, A., de Mendizabal, N.V., Betzel, R.F., Griffa, A., Hagmann, P., Corominas-Murtra, B., Thiran, J.-P., Sporns, O., 2014. Resting-brain functional connectivity predicted by analytic measures of network communication. Proc. Natl. Acad. Sci. U.S.A. 111, 833–838. doi:10.1073/pnas.1315529111.

Greicius, M.D., Supekar, K., Menon, V., Dougherty, R.F., 2009. Resting-state functional connectivity reflects structural connectivity in the default mode network. Cereb. Cortex 19, 72–78. doi:10.1093/cercor/bhn059.

Hagmann, P., Cammoun, L., Gigandet, X., Meuli, R., Honey, C., Wedeen, V.J., Sporns, O., 2008. Mapping the structural core of human cerebral cortex. PLoS Biol. 6, e159. doi:10.1371/journal.pbio.0060159.

Haufe, S., Nikulin, V.V., Müller, K.-R., Nolte, G., 2013. A critical assessment of connectivity measures for EEG data: a simulation study. Neuroimage 64, 120–133. doi:10.1016/j.neuroimage.2012.09.036.

van den Heuvel, M.P., Pol, H.E.H., 2010. Exploring the brain network: a review on resting-state fMRI functional connectivity. Eur. Neuropsychopharmacol. 20, 519–534. doi:10.1016/j.euroneuro.2010.03.008.

Hipp, J.F., Engel, A.K., Siegel, M., 2011. Oscillatory synchronization in large-scale cortical networks predicts perception. Neuron 69, 387–396. doi:10.1016/j.neuron.2010.12.027.

Hipp, J.F., Hawellek, D.J., Corbetta, M., Siegel, M., Engel, A.K., 2012. Large-scale cortical correlation structure of spontaneous oscillatory activity. Nat. Neurosci. 15, 884–890. doi:10.1038/nn.3101.

Hjorth, B., 1975. An on-line transformation of EEG scalp potentials into orthogonal source derivations. Electroenceph. Clin. Neurophysiol. 39, 526–530. doi:10.1016/0013-4694(75)90056-5.

Honey, C.J., Sporns, O., Cammoun, L., Gigandet, X., Thiran, J.-P., Meuli, R., Hagmann, P., 2009. Predicting human resting-state functional connectivity from structural connectivity. Proc. Natl. Acad. Sci. U.S.A. 106, 2035–2040. doi:10.1073/pnas.0811168106.

Honey, C.J., Thivierge, J.-P., Sporns, O., 2010. Can structure predict function in the human brain? Neuroimage 52, 766–776. doi:10.1016/j.neuroimage.2010.01.071.

Jenkinson, M., Bannister, P., Brady, M., Smith, S., 2002. Improved optimization for the robust and accurate linear registration and motion correction of brain images. Neuroimage 17, 825–841. doi:10.1016/s1053-8119(02)91132-8.

Jenkinson, M., Beckmann, C.F., Behrens, T.E.J., Woolrich, M.W., Smith, S.M., 2012. FSL. Neuroimage 62, 782–790. doi:10.1016/j.neuroimage.2011.09.015.

Jeurissen, B., Tournier, J.-D., Dhollander, T., Connelly, A., Sijbers, J., 2014. Multi-tissue constrained spherical deconvolution for improved analysis of multi-shell diffusion MRI data. Neuroimage 103, 411–426. doi:10.1016/j.neuroimage.2014.07.061.

Kellner, E., Dhital, B., Kiselev, V.G., Reisert, M., 2016. Gibbs-ringing artifact removal based on local subvoxel-shifts. Magn. Reson. Med. 76, 1574–1581. doi:10.1002/mrm.26054.

Koch, M.A., Norris, D.G., Hund-Georgiadis, M., 2002. An investigation of functional and anatomical connectivity using magnetic resonance imaging. Neuroimage 16, 241–250. doi:10.1006/nimg.2001.1052.

Lachaux, J.-P., Rodriguez, E., Martinerie, J., Varela, F.J., 1999. Measuring phase synchrony in brain signals. Hum. Brain Mapp. 8, 194–208. 10.1002/(SICI)1097-0193(1999)8:4<194::AID-HBM4>3.0.CO;2-C

Lancaster, G., Iatsenko, D., Pidde, A., Ticcinelli, V., Stefanovska, A., 2018. Surrogate data for hypothesis testing of physical systems. Phys. Rep. 748, 1–60. doi:10.1016/j.physrep.2018.06.001.

Le Bihan, D., Heidi, J.B., 2011. Diffusion MRI at 25: exploring brain tissue structure and function. Neuroimage 61, 324–341. doi:10.1016/j.neuroimage.2011.11.006.

Lesage, J.P., Olivier, P., 2007. Bayesian model averaging for spatial econometric models. Geogr. Anal. 39, 241–267. doi:10.1111/j.1538-4632.2007.00703.x.

Liu, X., Zhou, L., Ding, F., Wang, Y., Yan, J., 2015. Local field potentials are local events in the mouse auditory cortex. Eur. J. Neurosci. 42, 2289–2297. doi:10.1111/ejn.13003.

Marrelec, G., Messé, A., Giron, A., Rudrauf, D., 2016. Functional connectivity's degenerate view of brain computation. PLoS Comput. Biol. 12, e1005031. doi:10.1371/journal.pcbi.1005031.

Meier, J., Tewarie, P., Hillebrand, A., Douw, L., van Dijk, B.W., Stufflebeam, S.M., Mieghem, P.V., 2016. A mapping between structural and functional brain networks. Brain Connect. 6, 298–311. doi:10.1089/brain.2015.0408.

Mejias, J.F., Murray, J.D., Kennedy, H., Wang, X.J., 2016. Feedforward and feedback frequency-dependent interactions in a large-scale laminar network of the primate cortex. Sci. Adv. 2, e1601335. doi:10.1126/sciadv.1601335.

Messé, A., 2020. Parcellation influence on the connectivity-based structure-function relationship in the human brain. Hum. Brain Mapp. 41, 1167–1180. doi:10.1002/hbm.24866.

Messé, A., Benali, H., Marrelec, G., 2015. Relating structural and functional connectivity in MRI: a simple model for a complex brain. IEEE Trans. Med. Imaging 34, 27–37. doi:10.1109/TMI.2014.2341732.

Messé, A., Hütt, M.-T., Hilgetag, C.C., 2018. Toward a theory of coactivation patterns in excitable neural networks. PLoS Comput. Biol. 14, 1–19. doi:10.1371/journal.pcbi.1006084.

Messé, A., Rudrauf, D., Benali, H., Marrelec, G., 2014. Relating structure and function in the human brain: relative contributions of anatomy, stationary dynamics, and non-stationarities. PLoS Comput. Biol. 10, e1003530. doi:10.1371/journal.pcbi.1003530.

Messé, A., Rudrauf, D., Giron, A., Marrelec, G., 2015. Predicting functional connectivity from structural connectivity via computational models using MRI: an extensive comparison study. Neuroimage 111, 65–75. doi:10.1016/j.neuroimage.2015.02.001.

Mormann, F., Lehnertz, K., David, P., E Elger, C., 2000. Mean phase coherence as a measure for phase synchronization and its application to the EEG of epilepsy patients. Phys. D 144, 358–369. doi:10.1016/S0167-2789(00)00087-7.

Nolte, G., Bai, O., Wheaton, L., Mari, Z., Vorbach, S., Hallett, M., 2004. Identifying true brain interaction from EEG data using the imaginary part of coherency. Clin. Neurophysiol. 115, 2292–2307. doi:10.1016/j.clinph.2004.04.029.

Oostenveld, R., Fries, P., Maris, E., Schoffelen, J.M., 2011. FieldTrip: open source software for advanced analysis of MEG, EEG, and invasive electrophysiological data. Comput. Intel. Neurosc. 2011, 156869. doi:10.1155/2011/156869.

Palva, J.M., Palva, S., 2012. Discovering oscillatory interaction networks with M/EEG: challenges and breakthroughs. Trends Cogn. Sci. 16, 219–230. doi:10.1016/j.tics.2012.02.004.

Palva, J.M., Wang, S.H., Palva, S., Zhigalov, A., Monto, S., Brookes, M.J., Schoffelen, J.-M., Jerbi, K., 2018. Ghost interactions in MEG/EEG source space: a note of caution on inter-areal coupling measures. Neuroimage 173, 632–643. doi:10.1016/j.neuroimage.2018.02.032.

Park, H.-J., Friston, K., 2013. Structural and functional brain networks: from connections to cognition. Science 342, 1238411. doi:10.1126/science.1238411.

de Pasquale, F., Penna, S.D., Snyder, A., Marzetti, L., Pizzella, V., Romani, G., Corbetta, M., 2012. A cortical core for dynamic integration of functional networks in the resting human brain. Neuron 74, 753–764. doi:10.1016/j.neuron.2012.03.031.

Pesaran, B., Vinck, M., Einevoll, G.T., Sirota, A., Fries, P., Siegel, M., Truccolo, W., Schroeder, C.E., Srinivasan, R., 2018. Investigating large-scale brain dynamics using field potential recordings: analysis and interpretation. Nat. Neurosci. 21, 903–919. doi:10.1038/s41593-018-0171-8.

Raichle, M., 2010. Two views of brain function. Trends Cogn. Sci. 14, 180–190. doi:10.1016/j.tics.2010.01.008.

Rubehn, B., Bosman, C., Oostenveld, R., Fries, P., Stieglitz, T., 2009. A MEMS-based flexible multichannel ECoG-electrode array. J. Neural Eng. 6, 036003. doi:10.1088/1741-2560/6/3/036003.

Schmidt, M., Bakker, R., Shen, K., Bezgin, G., Diesmann, M., van Albada, S.J., 2018. A multi-scale layer-resolved spiking network model of resting-state dynamics in macaque visual cortical areas. PLoS Comput. Biol. 14, 1–38. doi:10.1371/journal.pcbi.1006359.

Schnitzler, A., Gross, J., 2005. Normal and pathological oscillatory communication in the brain. Nat. Rev. Neurosci. 6, 285–296. doi:10.1038/nrn1650.

Siegel, M., Donner, T., Engel, A.K., 2012. Spectral fingerprints of large-scale neuronal interactions. Nat. Rev. Neurosci. 13, 121–134. doi:10.1038/nrn3137.

Siems, M., Siegel, M., 2020. Dissociated neuronal phase- and amplitude-coupling patterns in the human brain. Neuroimage 209, 116538. doi:10.1016/j.neuroimage.2020.116538.

Singer, W., 2013. Cortical dynamics revisited. Trends Cogn. Sci. 17, 616–626. doi:10.1016/j.tics.2013.09.006.

Sjøgård, M., Bourguignon, M., Costers, L., Dumitrescu, A., Coolen, T., Roshchupkina, L., Destoky, F., Bertels, J., Niesen, M., Ghinst, M.V., van Schependom, J., Nagels, G., Urbain, C., Peigneux, P., Goldman, S., Woolrich, M.W., De Tiège, X., Wens, V., 2020. Intrinsic/extrinsic duality of large-scale neural functional integration in the human brain. bioRxiv doi:10.1101/2020.04.21.053579.

Smith, S., Nichols, T., Vidaurre, D., Winkler, A., Behrens, T., Glasser, M., Ugurbil, K., Barch, D., Essen, D.V., Miller, K., 2015. A positive-negative mode of population covariation links brain connectivity, demographics and behavior. Nat. Neurosci. 18, 1565–1567. doi:10.1038/nn.4125.

Sporns, O., 2014. Contributions and challenges for network models in cognitive neuroscience. Nat. Neurosci. 17, 652–660. doi:10.1038/nn.3690.

Stitt, I., Hollensteiner, K.J., Galindo-Leon, E., Pieper, F., Fiedler, E., Stieglitz, T., Engler, G., Nolte, G., Engel, A.K., 2017. Dynamic reconfiguration of cortical functional connectivity across brain states. Sci. Rep. 7, 8797. doi:10.1038/s41598-017-08050-6.

Straathof, M., Sinke, M.R., Dijkhuizen, R.M., Otte, W.M., 2019. A systematic review on the quantitative relationship between structural and functional network connectivity strength in mammalian brains. J. Cerebr. Blood Flow Metab. 39, 189–209. doi:10.1177/0271678X18809547.

Tenke, C.E., Kayser, J., 2012. Generator localization by current source density (CSD): implications of volume conduction and field closure at intracranial and scalp resolutions. Clin. Neurophysiol. 123, 2328–2345. doi:10.1016/j.clinph.2012.06.005.

Tewarie, P., Abeysuriya, R., Byrne, A., O'Neill, G.C., Sotiropoulos, S.N., Brookes, M.J., Coombes, S., 2019. How do spatially distinct frequency specific meg networks emerge from one underlying structural connectome? The role of the structural eigenmodes. Neuroimage 186, 211–220. doi:10.1016/j.neuroimage.2018.10.079.

Tewarie, P., Hillebrand, A., van Dellen, E., Schoonheim, M., Barkhof, F., Polman, C., Beaulieu, C., Gong, G., van Dijk, B., Stam, C., 2014. Structural degree predicts functional network connectivity: a multimodal resting-state fMRI and MEG study. Neuroimage 97, 296–307. doi:10.1016/j.neuroimage.2014.04.038.

Theiler, J., Eubank, S., Longtin, A., Galdrikian, B., Farmer, J.D., 1992. Testing for nonlinearity in time series: the method of surrogate data. Physica D 58, 77–94. doi:10.1016/0167-2789(92)90102-S.

Ton, R., Deco, G., Daffertshofer, A., 2014. Structure-function discrepancy: inhomogeneity and delays in synchronized neural networks. PLoS Comput. Biol. 10, 1–15. doi:10.1371/journal.pcbi.1003736.

Tononi, G., Sporns, O., Edelman, G., 1994. A measure for brain complexity: relating functional segregation and integration in the nervous system. Proc. Natl. Acad. Sci. U.S.A. 91, 5033–5037. doi:10.1073/pnas.91.11.5033.

Tournier, J.-D., Calamante, F., Connelly, A., 2012. MRtrix: diffusion tractography in crossing fiber regions. Int. J. Imaging Syst. Technol. 22, 53–66. doi:10.1002/ima.22005.

Tustison, N.J., Avants, B.B., Cook, P.A., Zheng, Y., Egan, A., Yushkevich, P.A., Gee, J.C., 2010. N4ITK: improved N3 bias correction. IEEE Trans. Med. Imaging 29, 1310–1320. doi:10.1109/TMI.2010.2046908.

Uhlhaas, P., Singer, W., 2012. Neuronal dynamics and neuropsychiatric disorders: toward a translational paradigm for dysfunctional large-scale networks. Neuron 75, 963–980. doi:10.1016/j.neuron.2012.09.004.

Veraart, J., Novikov, D.S., Christiaens, D., Ades-aron, B., Sijbers, J., Fieremans, E., 2016. Denoising of diffusion MRI using random matrix theory. Neuroimage 142, 394–406. doi:10.1016/j.neuroimage.2016.08.016.

Vezoli, J., Vinck, M., Bosman, C.A., Bastos, A.M., Lewis, C.M., Kennedy, H., Fries, P., 2021. Brain rhythms define distinct interaction networks with differential dependence on anatomy. Neuron 109, 3862–3878.e5. doi:10.1016/j.neuron.2021.09.052.

Vincent, J.L., Patel, G.H., Fox, M.D., Snyder, A.Z., Baker, J.T., Van Essen, D.C., Zempel, J.M., Snyder, L.H., Corbetta, M., Raichle, M.E., 2007. Intrinsic functional architecture in the anaesthetized monkey brain. Nature 447, 83–86. doi:10.1038/nature05758.

Wang, S.H., Lobier, M., Siebenhühner, F., Puoliväli, T., Palva, S., Palva, J.M., 2018. Hyperedge bundling: a practical solution to spurious interactions in MEG/EEG source connectivity analyses. Neuroimage 173, 610–622. doi:10.1016/j.neuroimage.2018.01.056.

Wilson, H.R., Cowan, J.D., 1972. Excitatory and inhibitory interactions in localised populations of model neurons. Biophys. J. 12, 1–24. doi:10.1016/S0006-3495(72)86068-5.

Wirsich, J., Ridley, B., Besson, P., Jirsa, V., Bénar, C., Ranjeva, J.-P., Guye, M., 2017. Complementary contributions of concurrent EEG and fMRI connectivity for predicting structural connectivity. Neuroimage 161, 251–260. doi:10.1016/j.neuroimage.2017.08.055.